FINITE ELEMENT STRUCTURAL ANALYSIS TOWARDS THE STRUCTURAL HEALTH MONITORING OF A REMOTELY PILOTED AIRCRAFT WING SPAR

Dioser dos Santos
Tiago dos Santos
dioser.santos@gmail.com
tsantos.mec@gmail.com
Departamento de Engenharia Mecânica, Universidade Federal de Santa Maria
1000 Roraima Ave., 97105-900, Santa Maria, Rio Grande do Sul, Brazil

Abstract. *This paper covers a numerical analysis with the purpose of building a trustworthy model for predicting location and magnitude of critical stresses in an Unmanned Aerial Vehicle, based on telemetry generated flight parameters. This work is part of a greater effort in introducing the concept of Structural Health Monitoring into the Remotely Piloted Aircraft industry, with the main goal of providing safer operational conditions for associated equipment. In this sense, an analytical development is carried to estimate air loads to be applied to a finite element model of a UAV wing. The numerical analysis is intended to identify maximum stresses and corresponding locations at the wing spars, depending on flight conditions. Three different load cases are considered, based on distinct combinations of flight parameters. Two of these conditions represent critical situations known from the design process. The other one is an intermediate case, obtained from a set of flight data acquired by a telemetry system. This sort of analysis is important for knowing critical spots in the structure for further developments regarding in situ Structural Health Monitoring.*
Keywords: *Remotely Piloted Aircraft, Structural Health Monitoring, Finite Element Analysis.*

INTRODUCTION

The demand for more reliable Unmanned Aerial Systems is increasing in the world, following the market expansion of Remotely Piloted Aircraft (*RPA*) and related services. We frequently hear or read about new solutions using drones, most of them related to remote sensing and/or photogrammetry (Colomina et al., 2014; Senthilnath et al., 2017), but there are also unusual, more specific applications, such as 3D mapping for civil engineering projects (Siebert et al., 2014), routing of Vehicular Ad hoc Networks (Oubbati et al., 2017) and even metrology applications (Daakir et al., 2017). In Brazil, as in other countries across the globe, there is a great concern regarding safety issues associated with both air space operations and ground facilities related to such equipment. The importance of developing reliable systems and assuring continuous structural airworthiness has been emphasized by Kressel et al. (2014), whose work applied the concept of Structural Health Monitoring to a long endurance UAV.

Mainly inspired by the studies carried by Molent et al. (2000) – where the overall process of fatigue monitoring of jet fighter aircraft is reviewed – and Kressel et al. (2014), this paper is the beginning step towards a structural health monitoring system for a light category of remotely piloted aircraft. Based on previous research, it is clear that monitoring, modeling and control of aeronautical structures are still subjects of great interest in research and development, either from experimental and prediction of structural behavior points of view.

Structural analysis and experimental validation are still not common practices in the development of light category unmanned aircraft, which should not be a problem when they are designated for low range and altitude performance, working with small payloads. In contrast, as the corresponding operational requirements are increased, it is necessary that they be able to withstand a wider variety of load conditions for longer service periods. Reasoning on this fact, this paper aims at studying a remotely piloted aircraft used for remote sensing of plantations. During these service situations, an aircraft undergoes innumerous distinct loading conditions and performs multiple maneuvers, since it must cover an area of approximately 30,000 m² during operation. The system in question is the AT-190 shown in Figure 1, an Unmanned Aerial System produced by Auster Tecnologia Company.

Figure 1 - AT-190 Unmanned Aerial Vehicle

Aiming at providing a consistent engineering analysis, a theoretical approach is used to estimate the different loads imposed on the wing framework. The loading analysis considers distinct combinations of flight conditions, which are assessed by means of V-n maneuver diagram and experimental measurements of flight parameters. Based upon the evaluated structural loads, critical points (also called hot spots) in the wing spars and their corresponding stress levels are evaluated by means of finite element analysis. The resulting information is important for understanding the mechanical behavior of the wing airframe before extending this analysis approach towards a Structural Health Monitoring Program in further studies.

The analysis carried in this paper aims to build a trustworthy model for predicting location and magnitude of critical stresses and strains in an Unmanned Aerial Vehicle, based on telemetry generated flight parameters. The engineering approach used for a complete structural health monitoring process is shown in Figure 2, from which it is possible to observe that this paper is focused on the six first steps, ending with stress and strain estimates. In this sense, the subsequent development focus on defining the pertinent maneuver conditions, monitoring the corresponding flight parameters, and thus estimating the associated aerodynamic loads acting on the wing structure, which are then used to estimating the location and magnitude of the internal efforts undergone by the wing spar. These main results are important to a further *in situ* experimental Structural Health Monitoring process.

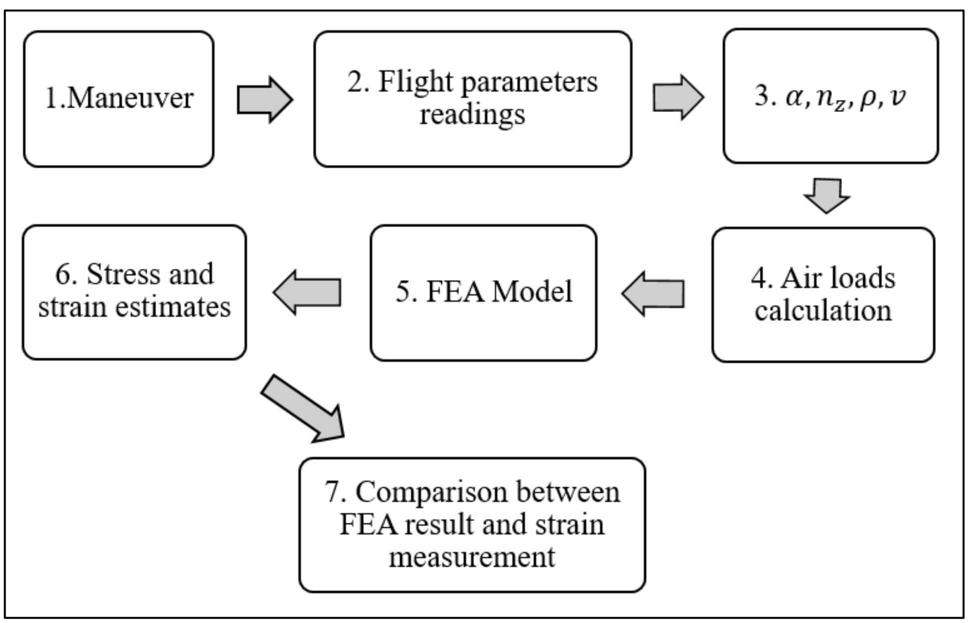

Figure 2 - Complete Structural Health Monitoring process; in step 3, α, n_z, ρ, v refer to angle of attack, normal load factor, air density and airspeed, respectively.

1. AERODYNAMIC LOADS CALCULATION

The main goal of calculating aerodynamic loads is to generate an accurate load model for the structural analysis using flight parameters that are accessible during normal operation of the aircraft. Those parameters are obtained from telemetry flight data records ordinarily used during the mission, regarding attitude, velocity and atmospheric conditions. Additionally, specific conditions within the maneuver envelope can be built in the load model to evaluate the structural behavior for critical circumstances.

It is desirable that the loads inserted in the numerical solution represent the condition under which the aircraft is flying as closely as possible. Modeling a pressure field around the wing surface is an interesting approach, as it accounts for the complex load distribution over the entire surface. Such approach has been used by Widmaier (2005) in the context of a composite structure optimization with good results, and is the preferred method for this study.

The aerodynamic loads model used for a symmetrical maneuver condition takes into consideration the following assumptions, according to Lomax (1996):

1) Airspeed remains constant during the maneuver
2) Roll and yaw accelerations are neglected during the maneuver

The steady-state system for the aircraft in a symmetrical maneuver is shown in Figure 3, from which Eq. (1) can be derived according to Lomax (1996),

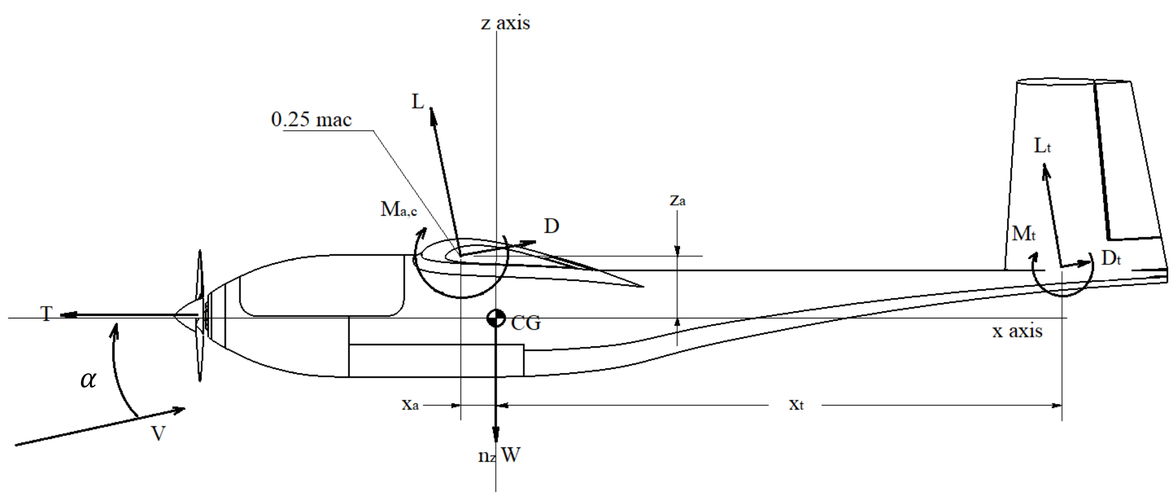

Figure 3 - Balancing loads in steady-state symmetrical maneuver

$$M_{a,c} + n_z W x_a + n_x W z_a = L_t x_t - M_t - T_{eng} z_e \quad (1)$$

where $M_{a,c}$ is the moment about the aerodynamic center of the wing, n_z is the load factor in the vertical axis of the aircraft, W the weight, x_a the distance between the aerodynamic center of the wing and the center of gravity in the longitudinal axis. n_x is the load factor in the x direction, z_a is the distance between the aerodynamic center of the wing and the center of gravity in the vertical axis. L_t is the tail lift force, x_t is the tail moment arm, M_t refers to the moment about the tail aerodynamic center, T_{eng} and z_e (not shown in the picture) are thrust force delivered by the electric motor and its respective distance to the center of gravity in the vertical direction.

The distance x_a can be determined using Eq. (2),

$$x_a = (x_{CG} - 0.25) \cdot c_w \tag{2}$$

where x_{CG} and c_w are relative position of the center of gravity and wing chord, respectively.

The global lift coefficient the aircraft produces when performing a symmetrical maneuver of load factor n_z is calculated with Eq. (3),

$$C_{L,global} = \frac{n_z W}{q\, S_w} \tag{3}$$

where q is the dynamic pressure and S_w is the wing reference surface.

And pitching moment about the aerodynamic center is

$$M_{a,c} = C_{M,ac}\, q\, S_w c_w \tag{4}$$

with $C_{M,ac}$ being the wing moment coefficient.

Substituting Eq. (2, 3, 4) in Eq. (1) and solving for L_t gives

$$L_t = \left[(x_{cg} - 0.25) C_{L,global} + C_{M,ac}\right] \frac{q S_w c_w + M_t + T_{eng} z_e + n_x W z_a}{x_t} \tag{5}$$

Figure 3 shows that the engine line is approximately coincident with the center of gravity location, so it is reasonable to neglect thrust effects in the balance equation. The moment of the tail about its aerodynamic center is also very small, as it uses a symmetrical airfoil, making it possible to consider it as zero. Considering that there is no expressive acceleration in the longitudinal direction leads to Eq. (6).

$$L_t = \left[(x_{CG} - 0.25) C_{L,global} + C_{M,ac}\right] \frac{q S_w c_w}{x_t} \tag{6}$$

According to Raymer (2006), the moment coefficient for a finite wing about its aerodynamic center can be calculated with Eq. (7) using the airfoil moment coefficient for the angle of attack in the flight condition.

$$C_{M,ac} = \frac{c_m (AR \cdot \cos(\Delta)^2}{(AR + 2\cos(\Delta))} \tag{7}$$

c_m is the airfoil moment coefficient, AR is the wing aspect ratio and Δ the sweep angle (in this concept it is zero). The graph in Figure 4 shows the aspect of moment coefficients either for airfoil and finite wing in function of angle of attack.

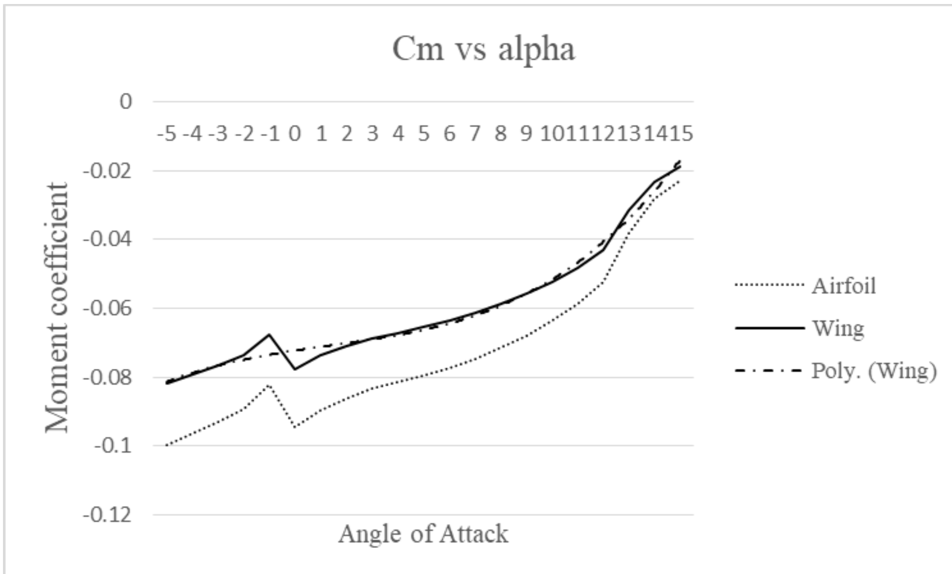

Figure 4 - Airfoil and wing moment coefficients

For each angle of attack, a different value of moment coefficient is given to Eq. (7), which can therefore be solved to find the value of tail downforce produced during the maneuver.

The wing lift force and lift coefficient of the wing during the maneuver are calculated using Eq. (8,9).

$$L = n_z W - L_t \tag{8}$$

$$C_{L,W} = \frac{2\,L}{q\,S_W} \tag{9}$$

Schrenk (1940) developed a simple but reliable method for predicting lift distribution of straight, high aspect ratio wings. Such method considers that the lift distribution aspect in a general planform wing is simply the average between its chord function and the elliptical wing chord function in the spanwise direction. If Schrenk Distribution is used for estimating lift coefficients across the wingspan and the pressure coefficient distribution in the chordwise direction is known, we can consider that there is a function $c_p(y, x)$ that defines a pressure field around the wing surface. The pressure coefficients of the airfoil, as shown in Figure 5, were obtained through the XFoil software and were evaluated for multiple lift coefficients, ranging from zero to 1.6 so we can model pressure distribution according to the wing lift coefficient.

$$c_p(y, x) = S(y) * p(x) \tag{10}$$

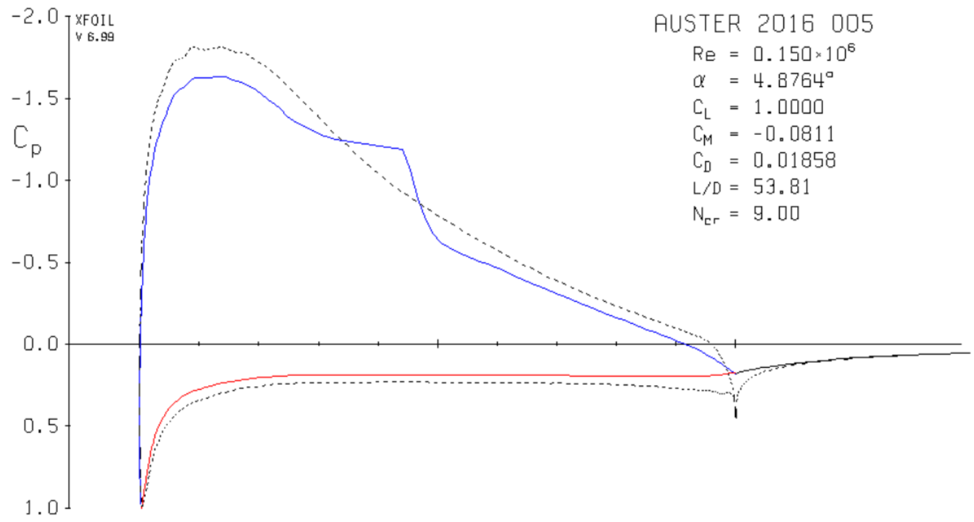

Figure 5 - Pressure coefficient plot for unit lift coefficient

Pressure coefficients are then multiplied by the Schrenk distribution value at the evaluated section, meaning that pressure distribution is "scaled down" to any local lift coefficient. As a result, a grid of pressure points is generated along the wing surface coordinates, enabling exportation to a finite element model analysis. Figure 6 shows the graphical aspect of Eq. (10).

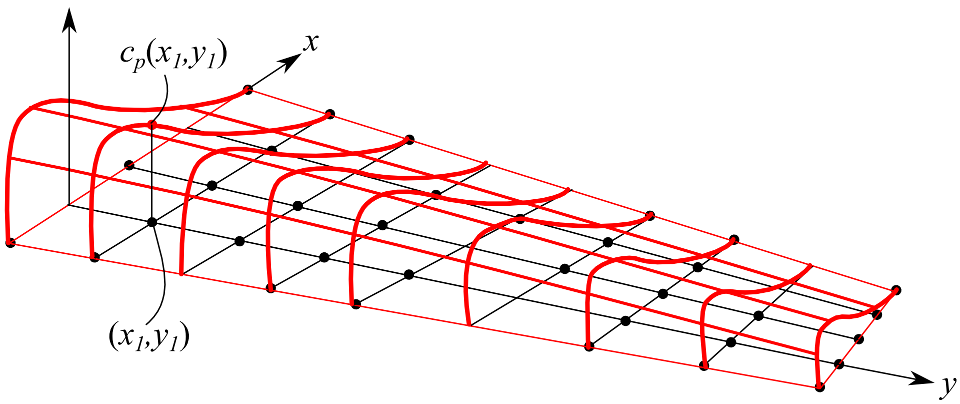

Figure 6 – Schematic pressure distribution representation around the wing surface

Flight conditions of interest for the analysis are provided by the V-n maneuver diagram for the aircraft, as shown in Figure 7. Each point shown in the envelope refers to a specific condition analyzed in this paper.

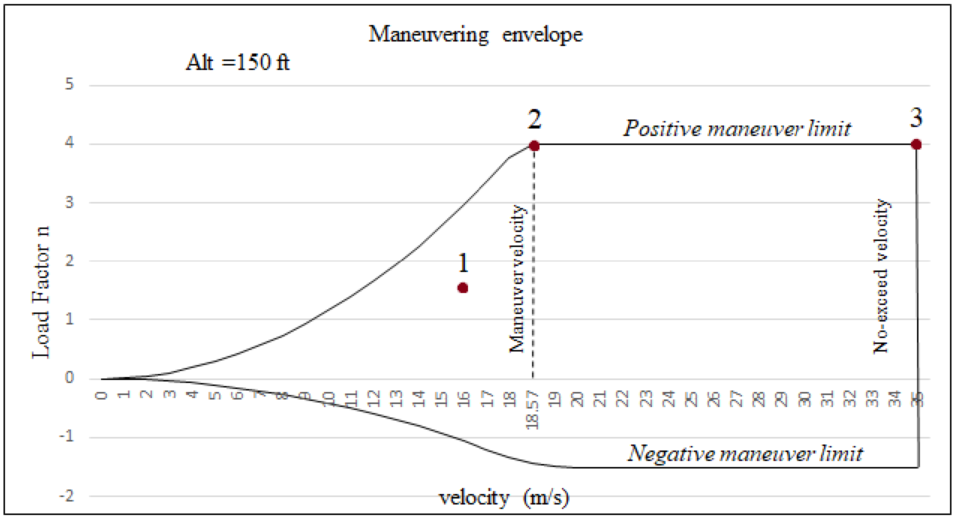

Figure 7 - Maneuvering envelope

Case number one is a set of flight parameters randomly picked from the record of flight data shown in Figure 8, which has been collected during the aircraft operation. An airspeed of 16 m/s and a 1.6 load factor correspond to this first load case.

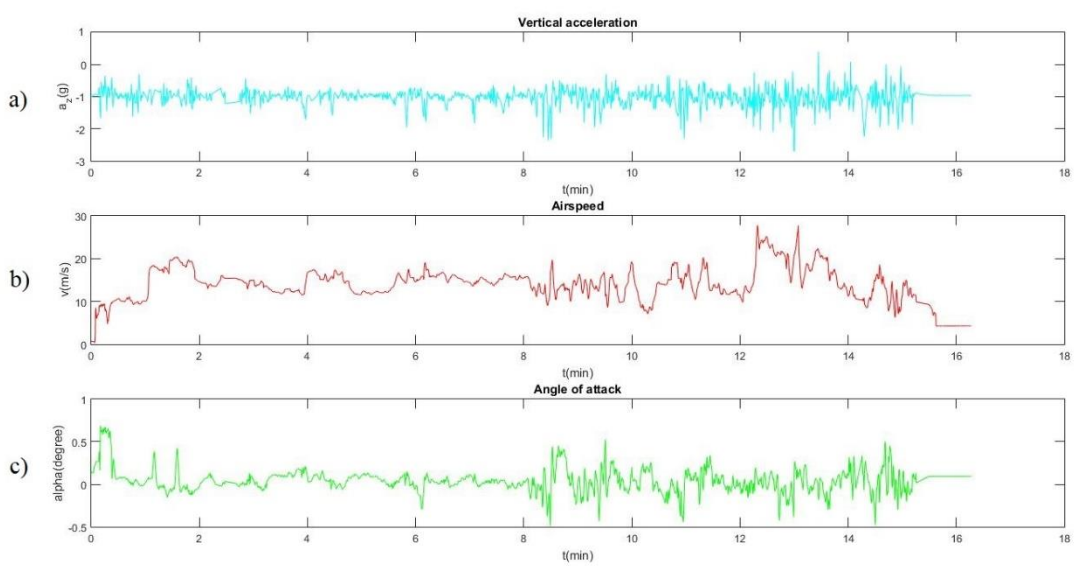

Figure 8 - Flight data obtained through flight testing; a) Vertical acceleration (g); b) Airspeed (m/s); c) Angle of attack (degrees); All parameters set in a time scale (min)

The flight conditions number two and three in Figure 7 correspond to critical situations known from the design process. The limit load factor for such situations is known as 4 from previous tests where the airplane was submitted to dive recovery maneuvers. Flight condition two happens when the aircraft performs a maneuver at the maximum angle of attack, at the maneuver speed, calculated as 18.57 m/s. The third condition is set when the aircraft is flying at its operational limit speed, also named no-exceed speed, or dive speed, which is known from flight tests to be equal to 35 m/s. In such condition the limit load factor is attained at a lower angle of attack due to the higher velocity. The loading conditions are summarized in Table 1.

Table 1 - Flight parameters for each condition

Loading case	Load factor	Angle of attack (degrees)	Airspeed (m/s)
1	1.6	2.8	16
2	4	15	18.57
3	4	0.5	35

2. FINITE ELEMENT MODEL

The finite element analysis has been carried in the Abaqus software using a half wing assembly model as shown in Figure 9. The fiberglass wing skin, shown in Figure 9 (A), was split in two main partitions, the outboard and the inboard surface, for applying the pressure fields. The spars in Figure 9 (B) are made of 6061 T6 aluminum alloy, with a tubular cross section. The fuselage part and wing ribs, shown in Figure 9 (C) and (D), respectively, are made of the same fiberglass laminate as the wing skin. The fuselage part was included in the analysis only for holding boundary conditions and a contact interaction with the spars, while the ribs are supposed to transmit the loads from the wing skin to the spars.

The properties of the materials used in the model are shown in Table 2 and Table 3.

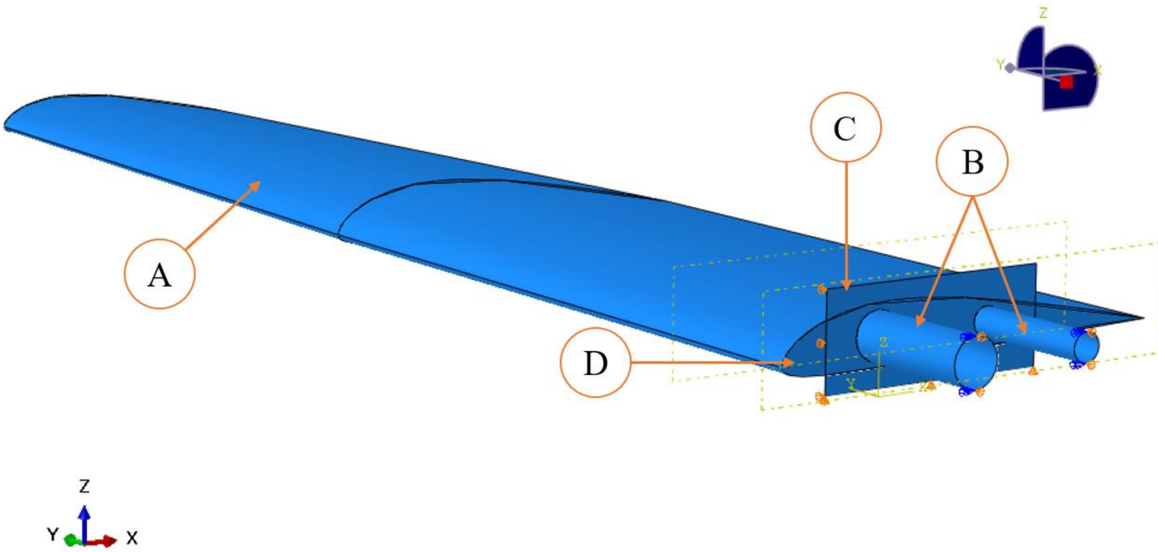

Figure 9 - Half-wing model; A) Wing skin; B) Spars; C) Fuselage part; D) Rib

Table 2 - Fiberglass-Epoxi composite mechanical properties

Property	(MPa)	Strength properties	(MPa)
E_X	26270	$\bar{\sigma}_{x,T}$	496.42
E_Y	8000	$\bar{\sigma}_{y,T}$	158.58
G_{XY}	3650	$\bar{\sigma}_{x,C}$	496.42
ν_{XY} (no unit)	0.26	$\bar{\sigma}_{y,C}$	158.58
Density (g/cm^3)	1.65	$\bar{\tau}_{x,y}$	75.84

The properties in Table 2 were taken from the material datasheet provided by the composites supplier E-Composites. E_X and E_Y are the moduli of elasticity in the longitudinal and transversal directions of the composite laminae, respectively. G_{XY} and ν_{XY} are in-plane shear modulus and Poisson's ratio, respectively. $\bar{\sigma}_{x,T}$ and $\bar{\sigma}_{y,T}$ are maximum tensile stresses in the longitudinal and transversal directions. $\bar{\sigma}_{x,C}$ and $\bar{\sigma}_{y,C}$ are maximum compressive stresses in the longitudinal and transversal directions. $\bar{\tau}_{x,y}$ is the in-plane shear strength of the lamina.

Table 3 - 6061-T6 Aluminum alloy mechanical properties

Property	(MPa)
Modulus of elasticity	68900
Poisson's ratio	0.33
Yield strength	276
Shear strength	207

The aluminum properties shown in Table 3 were found in the Matweb website.

The parts were modeled with the shell elements shown in Table 4, due to their relatively small thicknesses. The spars, for instance, have a wall thickness of 1 mm, whereas all the composite built parts, i.e., skin, ribs and fuselage part are 0.9 mm thick.

Table 4 - Elements used in each part

Part	Element type	Number of elements
Wing skin	S4R linear quadrilateral	4272
Main spar	S4R linear quadrilateral	37683
Secondary spar	S4R linear quadrilateral	3629
Fuselage portion	STRI65 quadratic triangular	2987
Wing rib	S3 linear triangular	108

The S4R is a 4-node, quadrilateral, stress/displacement shell element with reduced integration and a large-strain formulation, with six degrees of freedom per node and linear interpolation. The S3 is a linear 3-node triangular general-purpose shell, with finite membrane strains and six degrees of freedom for each node. The STRI65 element is a 6-node triangular thin shell, using five degrees of freedom per node and quadratic interpolation.

An overview of the complete mesh model is presented in Figure 10. A finer mesh has been applied to the wing main spar due to the fact that it carries most of the air loads and it also has interaction with the fuselage portion. The spar mesh was adjusted to a point where no significant differences in result could be identified. The wing skin and both spars received the S4R element, as shown in Figure 10 (A). It was noticed that when the fuselage mesh was coarse, it would lead to generating a deformed mesh in the spars. That was assumed to be caused by the assembly interactions existent in the region with the spars, so the fuselage part received a fine mesh as well, which eliminated the issue. The element used in Figure 10 (B) is the STRI65. The wing ribs are not points of interest, so they were modeled with a coarse mesh using the S3 element, as seen in Figure 10 (C).

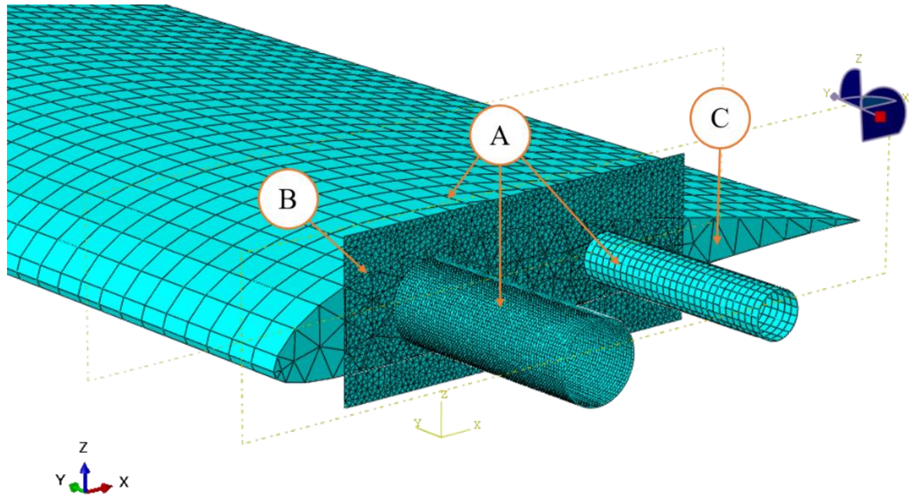

Figure 10 - Mesh generation in the model; A) S4R linear quadrilateral shell element; B) STRI65 quadratic triangular shell element; C) S3 linear triangular shell element

The pressure distribution around the wing surface was created as a mapped analytical field in the model with data provided by an Excel spreadsheet, which proceeds to calculate the pressure grid with Eq. 10 shown in the first section. Figure 11 shows the pressure distribution around the wing surface for the first flight condition and it is possible to notice its similarity with the schematic representation in Figure 6. As expected from the pressure coefficient distribution shown in Figure 5, the pressure vectors in Figure 11 decrease in size from the leading edge of the wing to its trailing edge. The pressure distribution is different for each flight condition to be analyzed in the finite element model.

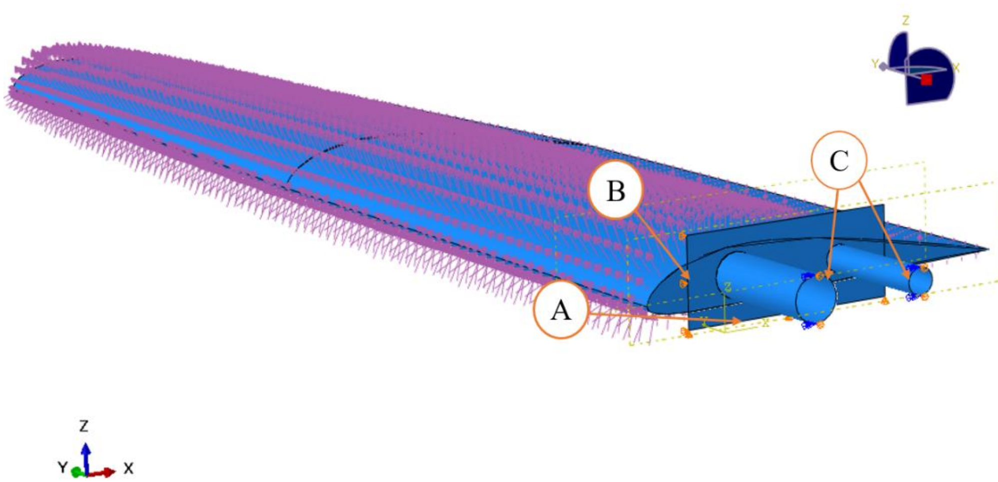

Figure 11 - Pressure distribution and boundary conditions; A) Vertical displacement constraint; B) Longitudinal displacement constraint; C) Symmetry boundary condition

The fuselage part was constrained in the vertical (z) and longitudinal (x) translations, shown in Figure 11 (A) and (B), respectively. Both spars were given the symmetric boundary condition shown in Figure 11 (C), i.e., constrained in the spanwise (y) translations and rotation around the longitudinal axis (x).

3. RESULTS AND DISCUSSION

The loading conditions obtained from the V-n Diagram in Figure 7 were applied to the model, resulting in the stresses shown in Figure 12, Figure **13** and Figure **14**. As the main kind of mechanical effect present in the system is the bending of the wing spars, the authors assumed to be more appropriate to analyze the structure in terms of its spanwise axial stress (S22). Subsequent strain measurements should be taken in that direction in order to simplify the finite element model validation. The maximum stresses are located at the top and bottom regions of the spar, however they are somewhat tilted in the counter-clockwise direction, as it can be seen from Figure 12, Figure 13 and Figure **14**.

For the first condition in the analysis (Figure 12), the resultant stresses were low, with a maximum compressive stress of approximately 22.40 MPa at the upper forward region of the main spar and a maximum tensile stress of 22.04 MPa at the opposite side.

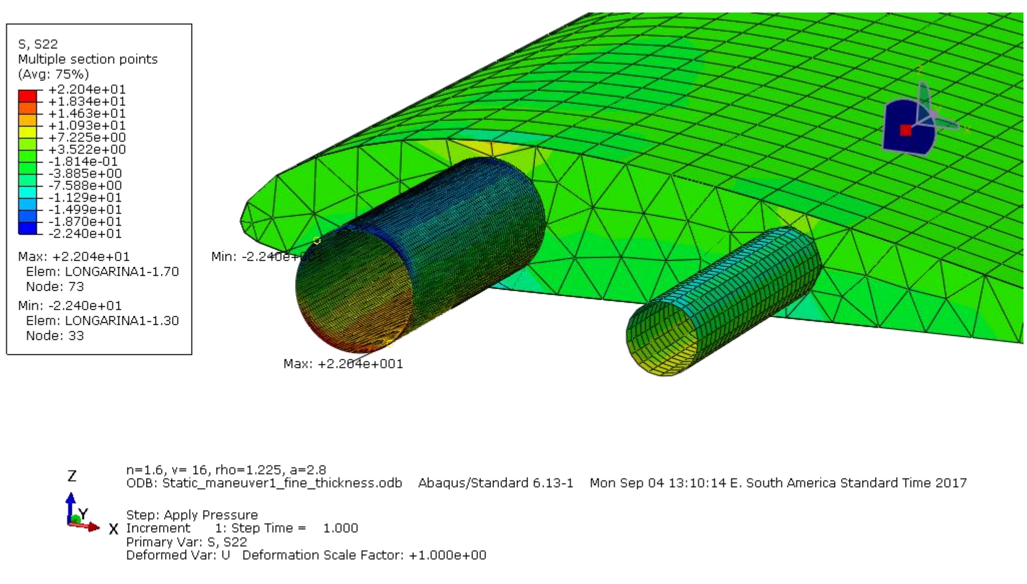

Figure 12 - Finite element analysis results for condition 1; Spanwise axial stress

For the second condition in the analysis (Figure 13), the higher load factor caused a significant increase in the stresses, with a maximum compressive stress of approximately 54.76 MPa at the upper forward region of the main spar and a maximum tensile stress of 53.89 MPa at the opposite side.

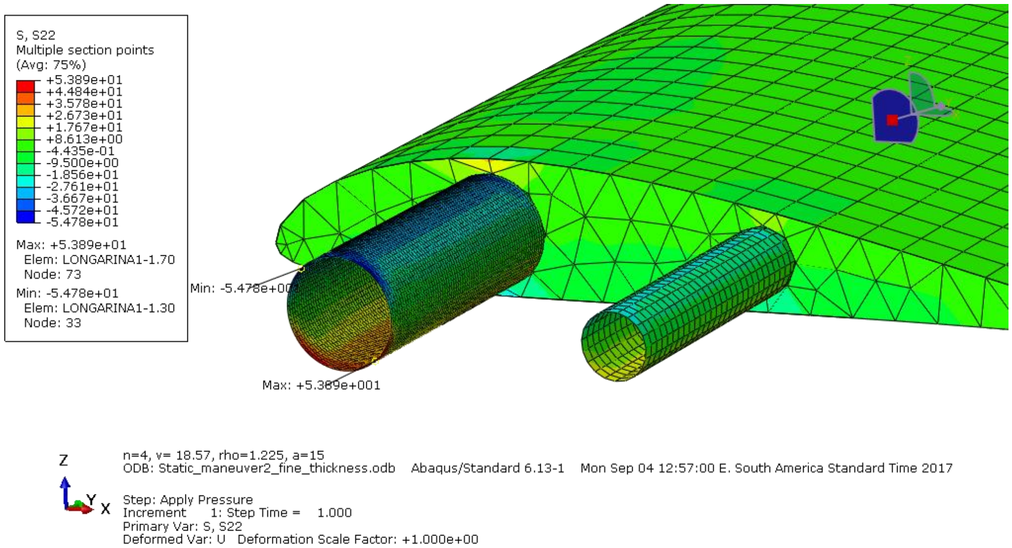

Figure 13 - Finite element analysis results for condition 2; Spanwise axial stress

The highest stresses result from the third condition (Figure 14), although they are not significantly greater than the previous analysis. The maximum compressive stress is approximately 57.38 MPa at the upper forward region of the main spar and the maximum tensile stress is 46.45 MPa at the opposite side. The results are summarized in Table 5.

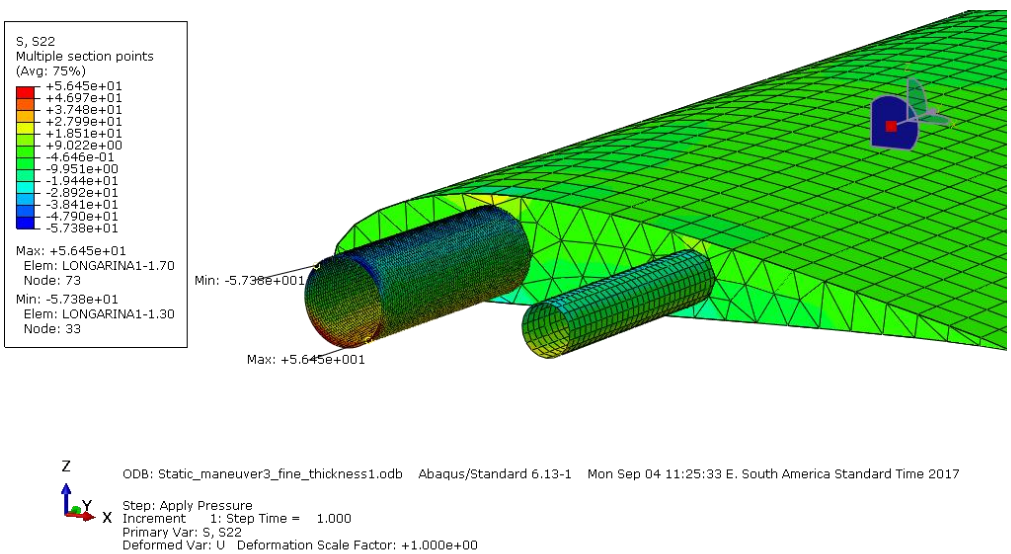

Figure 14 - Finite element analysis results for condition 3; Spanwise axial stress

Table 5 - Finite element analysis results

Loading case	Maximum axial stress (MPa)	Minimum axial stress (MPa)
1	22.04	-22.40
2	53.89	-54.78
3	56.45	-57.38

It can be seen from Figure 12, Figure **13**, Figure **14** and Table 5 that the critical loading condition happens when the aircraft is under maximum load factor, flying at the design limit speed, i.e., condition number three. Such condition is attainable during a recovery maneuver, as already measured in previous flight tests.

Even under critical loading conditions, stress still remains well bellow the material limit, which would allow either a change in section geometry or the use of a cheaper material in the production of the wing. Combining both solutions would give the best result, as it would reduce weight and cost of the component.

Knowing the approximate location of the maximum stresses is important for the subsequent studies that will be carried, where strain gauges will be placed on the hot spots for stress monitoring. Molent et al. (2000) comments that usually strain gauges are placed not in hot spots due to the multiple load paths existent in redundant aerospace structures, but in locations that allow airframe loads to be derived, and then used for calculating critical stresses. As the structures presented in this paper are simple, it would be no issue to place strain gauges directly on hot spots.

4. FUTURE DEVELOPMENTS

The first step towards further studies would be to place strain gauges on the hot spots identified in the finite element analysis, in order to validate the model. The flight parameters read by the on-board data acquisition system – primarily the ones shown in Figure 8 – may be directly used to calculate air loads in order to compare the FEA stress results against strain gauge-derived stresses. After validating the model, the further step would be to implement a cyclic damage counting method towards the in-flight structural health monitoring program.

In order to develop a future structural health monitoring system, strain histories must be monitored by a suitable data acquisition system. From the knowledge of associated elastic material parameters, the corresponding cyclic stress history can be calculated.

Regarding the structural life prediction task, when the cyclic load level oscillates during the fatigue process, a cumulative damage model can be employed. In this sense, the Palmgren-Miner rule is a widely used criterion to predict material fatigue life (see for instance Stephens et al., 2001):

$$\boldsymbol{D} = \sum \frac{\boldsymbol{n_j}}{\boldsymbol{N_j}} \tag{10}$$

Where $\boldsymbol{D}$ is the accumulated damage, $\boldsymbol{n_j}$ is the number of cycles applied at stress levels $\boldsymbol{\sigma_j}$ corresponding to a lifetime of $\boldsymbol{N_j}$. The failure is predicted when $\boldsymbol{D = 1}$. Thus, from the knowledge of the $\boldsymbol{S - N}$ curve related to the employed material, which must be inserted into the monitoring system, it is possible to instantaneously estimate the structural fatigue life, avoiding then eventual accidents. It is worth to mention that in such case, due to the existence of non null mean stresses, a suitable correction on the $\boldsymbol{S - N}$ curve, considering for example corrected Goodman criterion, must be performed.

5. CONCLUSIONS

A numerical analysis has been applied to identify critical spots and associated stress levels acting in an Unmanned Aerial Vehicle wing spar. As expected, such points were located at the wing root, although with stress levels lower than the material strength. As a consequence, design optimization is suggested to decrease weight and manufacturing cost of such structure. A detailed load model has been employed considering a full pressure distribution along the wing surface. This kind of approach accounts for various aerodynamic effects, such as lift, drag and twist moment, which is important for creating a trustworthy finite element model. Knowing the approximate location of the maximum stresses is important for the subsequent studies towards the development of a Structural Health Monitoring System to be implemented in the AT-190 remote sensing aircraft, produced by Auster Tecnologia. This study was the first step for the development of technology that can be extended to other applications, preventing accidents associated with the operation of unmanned aerial systems.

Acknowledgements

The authors are thankful to Auster Tecnologia members, who have been essential throughout the development of this paper.

REFERENCES

Colomina, I., Molina, P., 2014. Unmanned aerial systems for photogrammetry and remote sensing: A review. ISPRS Journal of Photogrammetry and Remote Sensing, vol. 92, pp. 79-97.

Daakir, M., Pierrot-Deseilligny, M., Bosser, P., Pichard, F., Thom, C., Rabot, Y., Martin, O., 2017. Lightweight UAV with on-board photogrammetry and single-frequency GPS positioning for metrology applications. ISPRS Journal of Photogrammetry and Remote Sensing, vol. 127, pp. 115-126.

E-Composites. Available at: < http://www.e-compostes.com>. Access in 17 jun. 2017.

Kressel, I. et al., 2014. High speed, in-flight structural health monitoring system for medium altitude long endurance unmanned air vehicle. 7th European Workshop on Structural Health Monitoring. La Cité, Nantes, France.

Lomax, T., 1996. Structural Loads Analysis for Commercial Transport Aircraft Theory and

Practice. American Institute of Aeronautics and Astronautics.
Matweb. Available at: < http://www.matweb.com>. Access in 21 mai. 2017.
Molent, L., Aktepe, B., 2000. Review of fatigue monitoring of agile military aircraft. Fatigue Fract. Engng. Mater. Struct., vol. 23, pp. 767-785.
Oubbati, O., Lakas, A., Zhou, F., Güne, M., Lagraa, N., Yagoubi, M., 2017. Intelligent UAV-assisted routing protocol for urban VANETs. Computer Communications, vol. 107, pp. 93-111.
Raymer, D. P., 2006. Aircraft design: a conceptual approach. American Institute of Aeronautics and Astronautics.
Schrenk, O., 1940; “A Simple Approximation Method for Obtaining the Spanwise Lift Distribution”, Technical Memorandums, National Advisory Committee for Aeronautics, Washington, USA.
Senthilnath, J., Kandukuri, M., Dokania, A., Ramesh, K., 2017. Application of UAV imaging platform for vegetation analysis based on spectral-spatial methods. Computers and Electronics in Agriculture, vol. 140, pp. 8-24.
Siebert, S., Teizer, J., 2014. Mobile 3D mapping for surveying earthwork projects using an Unmanned Aerial Vehicle (UAV) system. Automation in Construction, vol. 41, pp. 1-14.
Stephens, R. I.; Fatemi, A.; Stephens, R. R.; Fuchs, H. O., 2001. Metal Fatigue in Engineering. John Wiley & Sons, 2nd e.d.
Widmaier, K., 2005. Algoritmo genético aplicado à otimização de asas de material compósito de veículos aéreos não tripulados. Master’s dissertation, Universidade de São Paulo.